Wavenumber sampling strategies for 2.5-D frequency-domain seismic wave modelling in general anisotropic media

Bing Zhou,[1] Stewart Greenhalgh[1,2] and Mark Greenhalgh[3]

[1]*Department of Physics, School of Chemistry and Physics, The University of Adelaide,* SA 5005, *Australia.* E-mail: bing.zhou@adelaide.edu.au
[2]*Institute of Geophysics, ETH Zürich,* 8092 *Zürich, Switzerland*
[3]*Southern Geoscience Consultants Pty Ltd, Belmont,* WA 6104, *Australia*

SUMMARY

The computational efficiency of 2.5-D seismic wave modelling in the frequency domain depends largely on the wavenumber sampling strategy used. This involves determining the wavenumber range and the number of the sampling points, and overcoming the singularities in the wavenumber spectrum when taking the inverse Fourier transform to yield the frequency-domain wave solution. In this paper, we employ our newly developed Gaussian quadrature grid numerical modelling method and extensively investigate the wavenumber sampling strategies for 2.5-D frequency-domain seismic wave modelling in heterogeneous, anisotropic media. We show analytically and numerically that the various components of the Green's function tensor wavenumber-domain solutions have symmetric or antisymmetric properties and other characteristics, all of which can be fully used to construct effective and efficient sampling strategies for the inverse Fourier transform. We demonstrate two sampling schemes—called irregular and regular sampling strategies for the 2.5-D frequency-domain seismic wave modelling technique. The numerical results, which involve calibrations against analytic solutions, comparison of the different wavenumber sampling strategies and validation by means of 3-D numerical solutions, show that the two sampling strategies are both suitable for efficiently computing the 3-D frequency-domain wavefield in 2-D heterogeneous, anisotropic media. These strategies depend on the given frequency, elastic model parameters and maximum wavelength and the offset distance from the source.

Key words Numerical solutions; Body waves; Seismic anisotropy; Seismic tomography; Computational seismology; Wave propagation.

INTRODUCTION

In exploration seismology, if the geological structure is essentially 2-D then profiling measurements (surface reflection and refraction, offset VSP, cross-hole seismic) are usually taken perpendicular to the strike direction and used to image the subsurface. To process the field data and interpret the dynamic characteristics of the data, a 2-D wavefield modelling technique (e.g. finite difference, finite element) is frequently used (Kelley & Marfurt 1990) in which the point source used in practice is replaced by a line source. This brings mathematical simplicity to the problem and drastically reduces the computer memory and run time compared to full 3-D modelling. However, to make the synthetic data compatible with the observed data requires the application of special filters or correction procedures to convert the 3-D field data into line-source (2-D) data (Pratt 1999). Such filters are strictly only valid for simple homogeneous acoustic media in the far-field. They may be inaccurate at short range and when shear waves and multiple reflected phases are present. The situation is particularly acute when the arrivals overlap,

such as due to a strong velocity gradient. Williamson & Pratt (1995) quantify the error as being 35 per cent over a linear gradient region in which the velocity changes by a factor of two and caution against blind application of such filters. In fact, the filters were derived by comparing the asymptotic wavefield solutions for a point source and a line source in a uniform full-space. To overcome the drawbacks, or completely avoid making such 'corrections' or conversions, one may apply a 2.5-D seismic wave modelling technique (Pedersen *et al.* 1994; Song & Willamson 1995; Furumura & Takenka 1996; Pedersen *et al.* 1996; Zhou & Greenhalgh 1998a, b; Novais & Santos 2005; Sinclair *et al.* 2007) that accommodates the true point source and the 2-D model. The simulated wavefield then exhibits 3-D characteristics, which is much closer to the field situation than that with the line-source assumption and can be efficiently computed (Zhou & Greenhalgh 2006). This obviates the need for filter corrections but at the expense of increased computational effort. Recently, Roecker *et al.* (2010) demonstrated a 2.5-D teleseismic waveform tomography technique, for which they employed an optimal nine-point finite difference method to solve the 2.5-D elastic wave equation. They

GJI Seismology

showed the possibility to image the undulating Moho discontinuity using the teleseismic waveforms. However, they used a regular grid, an isotropic description of the rocks, and ignored the symmetric or antisymmetric property of the frequency-domain wavefields in the 2.5-D case. It is necessary to develop a more versatile technique that is more efficient in computation and has the capability to handle complex 2-D geological models involving anisotropic rocks and an arbitrary free-surface topography as often encountered in practice.

To implement non-linear seismic diffraction tomography (Gelius 1995), frequency-domain full-waveform inversion (Pratt 1999) and reverse-time migration using frequency-domain extrapolation (Xu *et al.* 2010), it is necessary to compute the frequency-domain wave solutions in the starting geological model and in the subsequent iterative updates. To obtain the frequency–space domain wave solution, one must compute the discrete inverse Fourier transform of the frequency–wavenumber domain wave solution for a series of wavenumber samples. Each wavenumber-domain solution is obtained by solving a large dimensional linear equation system. Our previous studies (Zhou & Greenhalgh 2006; Sinclair *et al.* 2007, 2011) have shown that there exist critical wavenumbers in both the acoustic and elastic cases at which the wavenumber spectral amplitudes become singular. The number of critical wavenumbers increases with the degree of anisotropy and the number of sub-volumes of the 2-D model. Determining the distributions of the wavenumber samples to avoid the singularities is therefore crucial to the 2.5-D modelling technique. The more the wavenumber samples that are employed, the greater the chance of encountering the singularities and the more expensive the computer time will be. Such problems seriously detract from the advantages of 2.5-D frequency-domain wave modelling. Therefore, we seek to develop an optimal wavenumber sampling strategy that may efficiently yield satisfactory frequency-domain wave solutions for non-linear diffraction tomography or frequency-domain full-waveform inversion in anisotropic media. This paper has this as its primary goal. We develop two wavenumber sampling strategies, called the irregular and the regular sampling strategies, respectively. Both fully apply the symmetric and antisymmetric properties and other characteristics of the wavenumber-domain solutions to significantly reduce the number of wavenumber samples required for the inverse Fourier transform. We also show that the two wavenumber sampling strategies are functions of the given frequency, elastic model parameters and maximum wavelength, as well as the source–receiver offset. The numerical results verify the applicability of the two strategies for computation of the frequency-domain wavefields in heterogeneous, anisotropic media.

The remainder of the paper is organized into five sections. The first section briefly gives the basic equations of the 2.5-D frequency-domain wave modelling technique. The second section analytically shows that the wavenumber-domain Green's function solutions are either symmetric or antisymmetric. The third section describes two wavenumber sampling strategies and demonstrates their advantages and disadvantages. The fourth section gives three numerical examples involving homogeneous and heterogeneous, isotropic and anisotropic media, which show the properties of the wavefield solutions and the effectiveness of the two sampling strategies. The final section draws some conclusions from this work.

BASIC EQUATIONS

The governing equation for 2.5-D frequency-domain seismic modelling is obtained by taking a spatial Fourier transform with respect to the *y*-coordinate (medium invariant direction for a 2-D model) of the 3-D frequency-domain wave equation. For a general anisotropic medium, the result can be stated as (Zhou & Greenhlagh 2010)

$$[\mathbf{D}_1(\omega, k_y, \tilde{\mathbf{m}}) + \mathbf{D}_2(\omega, k_y, \tilde{\mathbf{m}})]\overline{\overline{\mathbf{G}}}_s = -\hat{\mathbf{s}}\delta(\mathbf{r} - \mathbf{r}_s), \qquad (1)$$

where the vector $\tilde{\mathbf{m}} = (\tilde{\rho}, \tilde{c}_{ijkl})$ represents the model parameters which comprise the density $\tilde{\rho}$ and elastic moduli $\tilde{c}_{ijkl}$ of the medium; both are incorporated with the perfectly matched layers and are generally complex-valued functions of the *x*- and *z*-coordinates (Zhou & Greenhalgh 2011). The scalars ω and k_y in the above equation denote the frequency and the wavenumber, respectively, with the latter corresponding to the Fourier transform variable with respect to the *y*- (or strike) coordinate direction due to the 2-D nature of the geological model. The unit vector $\hat{\mathbf{s}}$ stands for the impressed force direction at the source location $\mathbf{r}_s = (x_s, 0, z_s)$, whereas the vector $\overline{\overline{\mathbf{G}}}_s$ is the doubly Fourier transformed spectra of the Green's function vector, which is equivalent to the displacement vector arising from a unit-vector source $\hat{\mathbf{s}} = (\hat{s}_1, \hat{s}_2, \hat{s}_3)$ in the model $\tilde{\mathbf{m}}(x, z)$. The differential operators $\mathbf{D}_1(\omega, k_y, \tilde{\mathbf{m}})$ and $\mathbf{D}_2(\omega, k_y, \tilde{\mathbf{m}})$ are defined by

$$\mathbf{D}_1(\omega, k_y, \tilde{\mathbf{m}})\overline{\overline{\mathbf{G}}}_s = \left[\frac{\partial}{\partial x_i} \left(\tilde{c}_{ijkl} \frac{\partial \overline{\overline{G}}_{sk}}{\partial x_l} \right) \right.$$
$$\left. + \left(\tilde{\rho}\omega^2 \delta_{jk} - \tilde{c}_{2jk2}k_y^2 \right) \overline{\overline{G}}_{sk} \right] \mathbf{e}_j,$$

$$\mathbf{D}_2(\omega, k_y, \tilde{\mathbf{m}})\overline{\overline{\mathbf{G}}}_s = \mathrm{i}k_y \left[\frac{\partial}{\partial x_i} \left(\tilde{c}_{ijk2}\overline{\overline{G}}_{sk} \right) + \tilde{c}_{2jkl} \frac{\partial \overline{\overline{G}}_{sk}}{\partial x_l} \right] \mathbf{e}_j. \qquad (2)$$

Here, the factor 'i' is the unit imaginary number. From the above definitions, it is not difficult to show that the operator $\mathbf{D}_1(\omega, k_y, \tilde{\mathbf{m}})$ is positive self-adjoint, namely

$$\int_\Omega \mathbf{u} \cdot \mathbf{D}_1(\omega, k_y, \tilde{\mathbf{m}})\mathbf{v}\, d\Omega = \int_\Omega \mathbf{v} \cdot \mathbf{D}_1(\omega, k_y, \tilde{\mathbf{m}})\mathbf{u}\, d\Omega, \qquad (3)$$

whereas $\mathbf{D}_2(\omega, k_y, \tilde{\mathbf{m}})$ is negative self-adjoint for any two vectorial functions $\mathbf{u}, \mathbf{v} \in C^1(\Omega)$ (see Zhou & Greenhalgh 1999):

$$\int_\Omega \mathbf{u} \cdot \mathbf{D}_2(\omega, k_y, \tilde{\mathbf{m}})\mathbf{v}\, d\Omega = - \int_\Omega \mathbf{v} \cdot \mathbf{D}_2(\omega, k_y, \tilde{\mathbf{m}})\mathbf{u}\, d\Omega. \qquad (4)$$

To solve eq. (1), we apply the principle of weighted residuals (Becker *et al.* 1983)

$$\int_\Omega \mathbf{W} \cdot [\mathbf{D}(\tilde{\mathbf{m}}, \omega, k_y)\overline{\mathbf{G}}_s + \hat{\mathbf{s}}\delta(\mathbf{r} - \mathbf{r}_s)]d\Omega = 0 \qquad (5)$$

for which we choose three basic weighting functions: $\mathbf{W}_1(\mathbf{r}) = [W(\mathbf{r}), 0, 0]$, $\mathbf{W}_2(\mathbf{r}) = [0, W(\mathbf{r}), 0]$, $\mathbf{W}_3(\mathbf{r}) = [0, 0, W(\mathbf{r})]$, where $W(\mathbf{r}) \in C^1(\Omega)$, and calculate the integration with a Gaussian quadrature grid (GQG). It leads to the following system of linear equations (for details, see Zhou *et al.* 2011)

$$\mathbf{M}(\omega, k_y, \tilde{\mathbf{m}})\overline{\overline{\mathbf{G}}}_s = \mathbf{b}_s, \qquad (6)$$

where $\overline{\overline{\mathbf{G}}}_s = (\overline{\overline{G}}_{sx1}, \overline{\overline{G}}_{sy1}, \overline{\overline{G}}_{sz1}, \overline{\overline{G}}_{sx2}, \overline{\overline{G}}_{sy2}, \overline{\overline{G}}_{sz2}, \ldots, \overline{\overline{G}}_{sxN}, \overline{\overline{G}}_{syN}, \overline{\overline{G}}_{szN})$ is the Green's function vector in the frequency-wavenumber domain, whose components are the vectorial values at each point of the GQG. The quantity N stands for the total number of points in the GQG. We simply call $\overline{\overline{\mathbf{G}}}_s$ the wavenumber-domain solution because of the dependence of the wavenumber k_y. The vector $\mathbf{b}_s = (0, 0, 0, \ldots, 0.\hat{s}_1, \hat{s}_2, \hat{s}_3, 0, \ldots 0, 0, 0)$ is the source vector whose components are zero except for the one at the source position. The matrix $\mathbf{M}(\omega, k_y, \tilde{\mathbf{m}})$ is a $3N \times 3N$ sparse matrix and

can be calculated for a given frequency ω, wavenumber k_y and set of model parameters $\tilde{\mathbf{m}} = (\tilde{\rho}, \tilde{c}_{ijkl})$. Solving eq. (6), one obtains the wavenumber-domain Green's function vector $\overline{\overline{\mathbf{G}}}_s$, from which the frequency-domain solution is obtained by inverse Fourier transforming over a range of wavenumber spectra:

$$\overline{\mathbf{G}}_s(\omega, x, y, z) = \frac{1}{2\pi} \int_{-\infty}^{\infty} \overline{\overline{\mathbf{G}}}_s(\omega, x, k_y, z) e^{ik_y y} dk_y$$

$$\approx \frac{k_y^c}{(\overline{N}_{ky} - 1)\pi} \sum_{j=1}^{\overline{N}_{ky}} \overline{\overline{\mathbf{G}}}_s(\omega, x, k_y^j, z) e^{ik_y^j y}. \tag{7}$$

Here k_y^c and $\overline{N}_{ky}$ are the cut-off wavenumber and the number of samples, respectively, and they define the wavenumber sampling strategy for eq. (7). $\overline{\overline{\mathbf{G}}}_s(\omega, x, k_y^j, z)$ are the wavenumber-domain solutions for the sequence $\{k_y^j \in [-k_y^c, k_y^c], j = 1, 2, \ldots, \overline{N}_{ky}\}$, which has a constant spacing $\Delta k_y = 2k_y^c/(\overline{N}_{ky} - 1)$. Eq. (7) shows that for one frequency-domain solution $\overline{\mathbf{G}}_s(\omega, x, y, z)$, it is necessary to solve the linear equation system (eq. 6) $\overline{N}_{ky}$ times. Therefore, the computational efficiency of 2.5-D wave modelling depends on the wavenumber sampling strategy used, which involves the determination of the cut-off value k_y^c and the number of wavenumber samples $\overline{N}_{ky}$. An ideal sampling strategy would be to keep $\overline{N}_{ky}$ as small as possible in the range $[-k_y^c, k_y^c]$ from which the Greens' function vector $\overline{\mathbf{G}}_s(\omega, x, y, z)$ can be satisfactorily obtained.

SYMMETRIES OF THE WAVENUMBER-DOMAIN SOLUTIONS

According to the definition of the inverse Fourier transform, eq. (7) can be rewritten in the following form:

$$\overline{\mathbf{G}}_s(\omega, x, y, z)$$

$$\approx \frac{k_y^c}{\pi N_{ky}} \begin{cases} \sum_{j=1}^{N_{ky}} \overline{\overline{\mathbf{G}}}_s(\omega, x, k_y^j, z) \cos(k_y^j y), & \overline{\overline{\mathbf{G}}}_s(k_y^j) \text{ is even,} \\ \sum_{j=1}^{N_{ky}} i\overline{\overline{\mathbf{G}}}_s(\omega, x, k_y^j, z) \sin(k_y^j y), & \overline{\overline{\mathbf{G}}}_s(k_y^j) \text{ is odd.} \end{cases} \tag{8}$$

This equation shows that if the wavenumber-domain solution $\overline{\overline{\mathbf{G}}}_s(\omega, x, k_y, z)$ is symmetric (even) or antisymmetric (odd) in wavenumber k_y, then one may employ half ($N_{ky} = \overline{N}_{ky}/2$) of the samples $\overline{\overline{\mathbf{G}}}_s(\omega, x, k_y^j, z)$, $k_y^j \in (0, k_y^c]$ to recover the frequency-domain solution $\overline{\mathbf{G}}_s(\omega, x, y, z)$. This means that the computational cost of 2.5-D wave modelling can be significantly reduced if the symmetries in the Green's function components occur. Accordingly, it is necessary to investigate the properties of the wavenumber-domain solutions $\overline{\overline{\mathbf{G}}}_s(\omega, x, k_y^j, z)$ in a heterogeneous, anisotropic medium.

If we designate $\overline{\overline{\mathbf{G}}}_s^+$ and $\overline{\overline{\mathbf{G}}}_s^-$ as the two wavenumber-domain solutions for positive $(+k_y)$ and negative $(-k_y)$ wavenumbers, respectively, we have the following identities according to eq. (1):

$$(\mathbf{D}_1 + \mathbf{D}_2^{|k_y|})\overline{\overline{\mathbf{G}}}_g^+ = -\hat{\mathbf{g}}\delta(\mathbf{r} - \mathbf{r_g}),$$

$$(\mathbf{D}_1 - \mathbf{D}_2^{|k_y|})\overline{\overline{\mathbf{G}}}_g^- = -\hat{\mathbf{g}}\delta(\mathbf{r} - \mathbf{r_g}), \tag{9}$$

where $\mathbf{D}_1 = \mathbf{D}_1(\omega, k_y, \tilde{\mathbf{m}})$ and $\mathbf{D}_2^{|k_y|} = \mathbf{D}_2(\omega, |k_y|, \tilde{\mathbf{m}})$, and the modulus symbol $|\cdot|$ around k_y denotes absolute value, $\hat{\mathbf{g}}$ is a unit vector located at receiver position $\mathbf{r}_g$. Multiplying $\overline{\overline{\mathbf{G}}}_s^+$ and $\overline{\overline{\mathbf{G}}}_s^-$ with the above equations, respectively, and integrating over the physical domain with the help of the positive and negative self-adjoint properties of the operators $\mathbf{D}_1$ and $\mathbf{D}_2$ (eqs 3 and 4), as well as the identity $(\mathbf{D}_1 + \mathbf{D}_2^{|k_y|})\overline{\overline{\mathbf{G}}}_{s,g}^+ = (\mathbf{D}_1 - \mathbf{D}_2^{|k_y|})\overline{\overline{\mathbf{G}}}_{s,g}^-$, we obtain

$$\overline{G}_{sg}^+ - \overline{G}_{sg}^- = 2 \int_\Omega \overline{\overline{\mathbf{G}}}_g \mathbf{D}_2^{|k_y|} \overline{\overline{\mathbf{G}}}_s \, d\Omega. \tag{10}$$

Setting $\hat{\mathbf{g}} = \hat{\mathbf{s}}$ in eq. (10) and recognizing that the right-hand side of the above equation becomes zero due to the negative self-adjoint property of $\mathbf{D}_2^{|k_y|}$ (see eq. 4), we have

$$\overline{\overline{G}}_{sg}^+ = \overline{\overline{G}}_{sg}^-, \quad \text{if } \hat{\mathbf{g}} = \hat{\mathbf{s}}. \tag{11}$$

This equation holds for any 2-D physical medium and shows the symmetries of the components of the wavenumber-domain Green's function vectors, that is, letting $\hat{\mathbf{s}} = \hat{\mathbf{g}} = \hat{\mathbf{x}}, \hat{\mathbf{y}}, \hat{\mathbf{z}}$ be the three unit vectors of the Cartesian coordinate system, it directly gives $\overline{\overline{G}}_{11}^+ = \overline{\overline{G}}_{11}^-$, $\overline{\overline{G}}_{22}^+ = \overline{\overline{G}}_{22}^-$, and $\overline{\overline{G}}_{33}^+ = \overline{\overline{G}}_{33}^-$. The subscripts 1, 2, 3 correspond to the three axis directions ($\hat{\mathbf{x}}, \hat{\mathbf{y}}, \hat{\mathbf{z}}$). In fact, the above relationships can be seen in Fig. 1, that is, as $\hat{\mathbf{s}} = \hat{\mathbf{g}} = \hat{\mathbf{x}}$, one can see the frequency-domain solution satisfies $\overline{G}_{11}(\omega, x, -y, z) = \overline{G}_{11}(\omega, x, y, z)$ due to the complete symmetries of the source ($\hat{\mathbf{s}}$) and geophone vectors ($\hat{\mathbf{g}}$), as well as the model parameters $\tilde{\mathbf{m}}(x, z)$ to the central plane ($y = 0$). So the wavenumber-domain solution $\overline{\overline{G}}_{11}(\omega, x, k_y, z)$ must be an even function of k_y in terms of eq. (8). Similarly, $\overline{\overline{G}}_{22}(\omega, x, k_y, z)$, $\overline{\overline{G}}_{33}(\omega, x, k_y, z)$, $\overline{\overline{G}}_{13}(\omega, x, k_y, z)$ and $\overline{\overline{G}}_{31}(\omega, x, k_y, z)$ are all symmetric which arises the off-diagonal components symmetric too, $\overline{\overline{G}}_{13}^+ = \overline{\overline{G}}_{13}^-$, $\overline{\overline{G}}_{31}^+ = \overline{\overline{G}}_{31}^-$. In addition, Fig. 1 also implies the following identities:

$$\overline{G}_{12}(\omega, x, y, z) = -\vec{G}_{12}(\omega, x, -y, z),$$

$$\overline{G}_{21}(\omega, x, y, z) = -\vec{G}_{21}(\omega, x, -y, z), \tag{12}$$

$$\overline{G}_{23}(\omega, x, y, z) = -\vec{G}_{23}(\omega, x, -y, z),$$

$$\overline{G}_{32}(\omega, x, y, z) = -\vec{G}_{32}(\omega, x, -y, z). \tag{13}$$

Accordingly, the wavenumber-domain solutions of the above components are antisymmetric: $\overline{\overline{G}}_{12}^+ = -\overline{\overline{G}}_{12}^-$, $\overline{\overline{G}}_{21}^+ = -\overline{\overline{G}}_{21}^-$, $\overline{\overline{G}}_{23}^+ =$
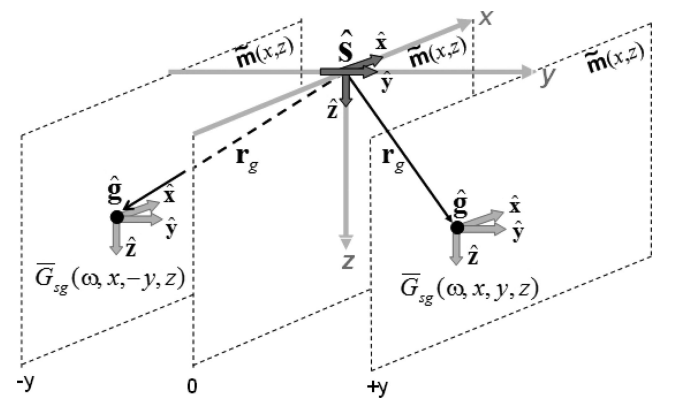

Figure 1. Symmetric properties of the 2.5-D seismic solutions with the given model parameters $\tilde{\mathbf{m}}(x, z)$ and source and geophone unit directional vectors $\hat{\mathbf{s}}$ and $\hat{\mathbf{g}}$.

$-\overline{\overline{G}}_{23}^-$ and $\overline{\overline{G}}_{32}^+ = -\overline{\overline{G}}_{32}^-$. In summary, we have established the following symmetric/antisymmetric properties for all components of the Green's function vectors in the wavenumber domain

$$\overline{\overline{G}}_{sg}^+ = (-1)^{s+g}\overline{\overline{G}}_{sg}^-, \quad (s, g = 1, 2, 3). \tag{14}$$

WAVENUMBER SAMPLING SCHEMES

Irregular strategy based on Gauss–Legendre sampling

We have shown that the components of the wavenumber-domain Green's function vector $\overline{\overline{\mathbf{G}}}_s(\omega, x, k_y, z)$ are either symmetric or antisymmetric. Accordingly, we can compute the frequency-domain solution $\overline{\mathbf{G}}_s(\omega, x, y, z)$ using the positive wavenumber samples $\{\overline{\overline{\mathbf{G}}}_s(\omega, x, k_y^j, z), \ k_y^j \in (0, k_y^c], j = 1, 2, \ldots, N_{ky}\}$. However, before sampling the wavenumber, we have to choose the cut-off value k_y^c, which can be determined from

$$k_y^c = \max\{k_p(\mathbf{r}) = \frac{\omega}{\sqrt{\mathrm{Re}\{\tilde{a}_{pp}(\mathbf{r})\}}}, \ p = 1, 2, \ldots, 6\} \tag{15}$$

for a heterogeneous anisotropic model. This equation was obtained from our previous research work on synthetic experiments using both analytic and numerical wave solutions that show any larger wavenumber than k_y^c has little contributions to the frequency-domain solutions except on receivers very close to the source (Zhou & Greenhalgh 2006; Sinclair *et al.* 2011). Here, $\tilde{a}_{pp}(\mathbf{r})$ are the diagonal elements of the Voigt recipes for up to 21 density-normalized elastic moduli. We called $k_p(\mathbf{r})$ the 'critical values' or 'singularities' of k_y at which the wavenumber-domain solution $\overline{\overline{\mathbf{G}}}_s(\omega, x, k_p, z)$ becomes infinite. Those 'critical points' or 'singularities' destroy the inverse Fourier transform and result in difficulties in being able to obtain the frequency-domain solution. To overcome the singularities, Zhou and Greenhalgh (2006) demonstrated a Gauss–Legendre sampling strategy for acoustic media, which essentially circumvented the critical points. From a methodology viewpoint, we may adapt such a sampling strategy to the case of a general anisotropic medium by investigating the characteristics of the wavenumber-domain solutions in anisotropic media, that is, we apply eq. (15) to calculate the singular points $k_p(\mathbf{r})$ that divide the wavenumber-domain $[0, k_y^c]$ into N_s^e effective intervals (which means that the two endpoints of the interval are not too close, that is, they must have more than 5 per cent change), and then apply the following formula to estimate the number of samples over the domain $(0, k_y^c]$:

$$N_{ky} = \sum_{q=1}^{N_s^e} \max\left\{5, \mathrm{int}\left[\Phi\left(\lambda_{\max}, r_{\max}, \Delta k_y^{(q)}\right)\right]\right\}. \tag{16}$$

The term $\max\{5, \mathrm{int}[\Phi(\lambda_{\max}, r_{\max}, \Delta k_y^{(q)})]\}$ gives the number of samples in the subdomain $[k_y^{(q-1)}, k_y^{(q)}]$, where $k_y^{(q)} \in \{k_p\}$; it has the minimum number of 5 but more likely is $\Phi(\lambda_{\max}, r_{\max}, \Delta k_y^{(q)})$, which generally depends on the maximum wavelength $\lambda_{\max} = max\{\sqrt{\mathrm{Re}(\tilde{a}_{pp})}\}/f$, the maximum source–receiver offset $r_{\max}$ and the effective interval $\Delta k_y^q = k_y^{(q)} - k_y^{(q-1)}$, where r is the offset distance from the source. In the acoustic case, $\Phi = 2r_{\max}/\lambda_{\max}$ and $N_s^e = 1$ (Zhou & Greenhalgh 2006). For general anisotropic media, we need to estimate this function in terms of the properties of the wavenumber-domain solutions (see the next section). After obtaining the number of samples $N_{ky}^{(q)} = \max\{5,\mathrm{int}[\Phi(\lambda_{\max}, r_{\max}, \Delta k_y^{(q)})]\}$ for the subdomain, we can analytically calculate the Gauss–Legendre weights $w_j^{(q)}$ and abscissa

values $k_y^j \in (k_y^{(q-1)}, k_y^{(q)})$, $j = 1, 2, \ldots, N_{ky}^{(q)}$ (Press *et al.* 1986) so that the inverse Fourier transform is computed by the formula

$$\overline{G}_{sg}(\omega, x, y, z)$$
$$= \sum_{q=1}^{N_s^e} \sum_{i=1}^{N_{ky}^{(q)}} \frac{\Delta k_y^q}{2\pi} w_i^q \begin{cases} \overline{\overline{G}}_{sg}(\omega, x, k_y^i, z)\cos(k_y^i y), & s+g = \text{even}, \\ i\overline{\overline{G}}_{sg}(\omega, x, k_y^i, z)\sin(k_y^i y), & s+g = \text{odd}, \end{cases}$$
$$\tag{17}$$

rather than using eq. (8). According to the distribution of the Gauss–Legendre abscissae k_y^j, the samples in each interval exclude the two endpoints of the interval $(k_y^{(q-1)}, k_y^{(q)})$ so that eq. (17) avoids the singularities on the positive k_y-axis. Therefore, the Gauss–Legendre sampling scheme is actually a singularity-skipping strategy. Due to the irregular distribution of the wavenumber samples (at the Gauss–Legendre points), we simply call it an irregular sampling strategy. However, from eq. (15) one finds that in a homogeneous, anisotropic medium there are in general six singularities due to the six diagonal elements $(a_{11}, a_{22}, a_{33}, a_{44}, a_{55}, a_{66})$. Even considering a tilted transversely isotropic medium (TTI-medium) that is a commonly used model in seismic exploration (Thomsen 1986), there may be four singularities in such a homogeneous model because $a_{11} = a_{22}$ and $a_{44} = a_{55}$. In a heterogeneous model consisting of N_m TTI media, one has to deal with $4N_m$ singularities distributed over $4N_m$ intervals covering the domain $(0, k_y^c]$. It is apparent that the singularity-skipping strategy is suitable for the case having a known certain number of singularities, but not suitable for the cases having an uncertain number of singularities. This would occur, for example, when implementing non-linear diffraction tomography or 2-D full-waveform inversion where the model parameters are successively upgraded with small quantities. Such an upgrading or adjustment procedure may cause many different numbers of singularities in the iterative inversions.

Regular strategy

As an alternative approach, it can be theoretically shown that the wavenumber singularities may be removed by introducing slight attenuation in the medium. This has been done for layered isotropic elastic media using complex velocities (or frequencies) in the Reflectivity method (see Mallick & Frazer 1987; Aki & Richards 2002, p. 393). For anisotropic media, one can employ six complex elastic moduli $\tilde{a}_{pp}^{(m)} = a_{pp}^{(m)} + i\varepsilon$ ($p = 1, 2, \ldots, 6$) in the mth subvolume of the model, where ε is a small quantity. Therefore, there are six complex wavenumbers $\tilde{k}_{mp} = \omega/\sqrt{\tilde{a}_{pp}^{(m)}}$ in solving eq. (1) so that the wavenumber samples k_y^j involved in the inverse Fourier transform are real valued quantities. The inverse Fourier transform therefore does not encounter any singularities along the real k_y axis because they are displaced off the positive k_y-axis in the complex plane $(k_{mp} \neq \tilde{k}_{mp})$. Our numerical experiments (see the next section) demonstrate the effectiveness of using complex wavenumbers—limiting the amplitudes of the samples $\overline{\overline{\mathbf{G}}}_s(\omega, x, k_y^j, z)$ and making the solutions continuous at the singularities. Accordingly, we can employ a sequence of wavenumbers uniformly or regularly distributed over the domain $(0, k_y^c]$, that is, $k_y^j = (j/N_{ky})k_y^c$, $j = 1, 2, \ldots N_{ky}$, where N_{ky} should be determined by the minimum spacing of the oscillations of the wavenumber-domain spectrum at the largest source–receiver offset and the highest frequency (see the next section). Unfortunately, we cannot know in advance the precise oscillatory nature of the wavenumber-domain solution and it
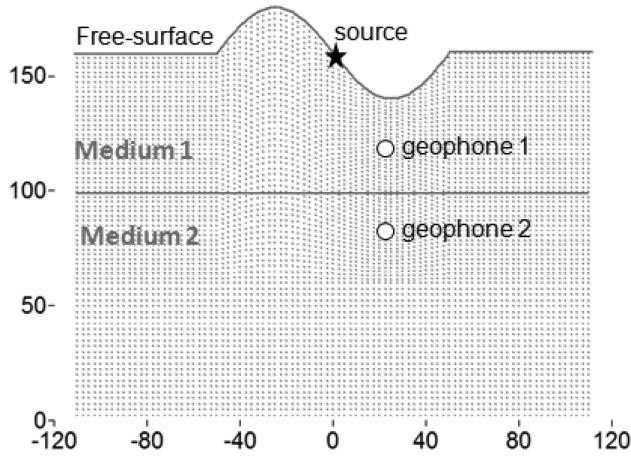
Figure 2. The synthetic model used for verification of the wavenumber sampling strategies. Medium 1 and Medium 2 are VTI media and their density-normalized elastic moduli are given in Table 1. The background to the plot is the Gaussian quadrature grid which samples the model parameters and the wavefield.

must be evaluated numerically for each model. Therefore, we may simply obtain N_{ky} by multiplying N_s^e to the estimate of max[5, int($2r_{max}/\lambda_{max}$)], namely,

$$N_{ky} = N_s^e \max\left[5, \text{int}\left(\frac{2r_{max}}{\lambda_{max}}\right)\right]. \tag{18}$$

This implies that the domain $(0, k_y^c)$ is divided into N_s^e equal parts and every part has the same distribution of sampling points. Note that in eq. (18) the quantity is the distance normalized by the wavelength, suggesting at least two samples per wavelength. After obtaining N_{ky}, one has the wavenumber sequence $k_y^j = jk_y^c/N_{ky}$ ($j = 1, 2, \ldots, N_{ky}$) that is used in eq. (6), and then eq. (8) is used to calculate the frequency-domain solution. Due to the uniform distribution of the wavenumber samples, we call this scheme the regular sampling strategy. It may be applied for non-linear seismic diffraction tomography or multiple-frequency full waveform inversion in which one hardly knows how many singularities will be involved and where the singularities are located in wavenumber space. This simple strategy enables us to completely ignore the singularity problem, but it is apparent that when a large number of N_s^e are employed much more computer time is taken up than with the irregular sampling strategy.

NUMERICAL EXPERIMENTS

To view the characteristics of the wavenumber-domain solutions, we set $f = 100$ Hz and solve eq. (6) to calculate the wavefields in a full-space homogeneous anisotropic model, whose spatial dimensions are 200 m × 200 m and discretized by means of 161 × 161 Gaussian quadrature abscissae. An analytic solution is available for such a model (Vavrycuk 2007) and may be employed to both validate and calibrate the wavenumber sampling strategies. Next we employed a second model comprising a two-layered anisotropic structure and incorporating an undulating surface topography (see Fig. 2) to verify the capability of the new sampling strategies. The elastic moduli of the two models are given in Table 1, along with the wavenumber singularities k_{mp}. From Table 1 it can be seen that both models have the cut-off wavenumber of $k_y^c = \max\{k_{mp}\} \approx 0.63$ and as the synthetic model changes from the uniform elastic full-space to the two-layered anisotropic structure, the number of wavenumber singularities increases from $N = 6$ to 16 over the wavenumber domain $[-k_y^c, k_y^c]$. Using these model parameters one can work out the minimum and maximum wavelengths in the models, that is, $\lambda_{min} \approx 10$ m and $\lambda_{max} \approx 25$ m, respectively, according to which the Gaussian quadrature point density $N_G = 9$ (the spatial sampling number for the minimum wavelength simulated in the model) is applied in the calculations. To avoid the singularities, a slight attenuation value of $\varepsilon = 10^{-12}$ is used.

Figs 3 and 4 show the real and imaginary parts of the spectra of the wavenumber-domain solutions at two different source–receiver offsets ($r = 28.3$ m, 212 m) in the two models. Diagrams (a) and (b) in each figure correspond to the two different offsets. One can see that Fig. 3 gives six pairs of diagrams for each offset. They represent the six independent components ($\overline{\overline{G}}_{11}, \overline{\overline{G}}_{12}, \overline{\overline{G}}_{13}, \overline{\overline{G}}_{22}, \overline{\overline{G}}_{23}, \overline{\overline{G}}_{33}$) of the three Green's function vectors $\mathbf{G_1} = (\overline{\overline{G}}_{11}, \overline{\overline{G}}_{12}, \overline{\overline{G}}_{13})$, $\mathbf{G_2} = (\overline{\overline{G}}_{21}, \overline{\overline{G}}_{22}, \overline{\overline{G}}_{23})$ and $\mathbf{G_3} = (\overline{\overline{G}}_{31}, \overline{\overline{G}}_{32}, \overline{\overline{G}}_{33})$, because of the equivalence of the components $\overline{\overline{G}}_{12} = \overline{\overline{G}}_{21}, \overline{\overline{G}}_{13} = \overline{\overline{G}}_{31}$ and $\overline{\overline{G}}_{23} = \overline{\overline{G}}_{32}$ due to complete symmetry of the full-space models and the vectors of the source and geophone. By comparison, Fig. 4 has nine diagrams representing nine independent components due to the presence of the free-surface topography, destroying the symmetry and leading to the inequalities $\overline{\overline{G}}_{12} \neq \overline{\overline{G}}_{21}, \overline{\overline{G}}_{13} \neq \overline{\overline{G}}_{31}$ and $\overline{\overline{G}}_{23} \neq \overline{\overline{G}}_{32}$. In each diagram we give two results obtained with $\overline{N}_{ky} = 128$ and $\overline{N}_{ky} = 512$ uniformly distributed wavenumber samples to view the global oscillatory behaviour in the wavenumber domain [–0.63, 0.63]. We use vertical dashed lines to indicate the locations of the singularities in each case. From these diagrams, we observe the following characteristics: (1) The numerical results demonstrate the symmetric or

Table 1. Synthetic models used for investigating the wavenumber sampling strategies.

| Synthetic model	Elastic moduli $a_{ij}^{\sim(m)} = a_{ij}^{(m)} + i\varepsilon$ ($\times 10^9 \, m^2 s^{-2}$)	Singularities $k_{mp} = \omega/\sqrt{\text{Re}(\tilde{a}_{pp}^{(m)})}$ ($f = 100$ Hz)
Full-space homogeneous anisotropic model (model-1)	$a_{11} = 6.25$, $a_{13} = 4.25$, $a_{33} = 6.25$, $a_{44} = 1.00$, $a_{66} = 2.25$	±0.25, ±0.42, ±0.63
Two-layered anisotropic model having a undulated surface topography (model-2)	$a_{11}^{(1)} = 4.00$, $a_{13}^{(1)} = 1.33$, $a_{33}^{(1)} = 5.00$, $a_{44}^{(1)} = 1.33$, $a_{66}^{(1)} = 1.94$. $a_{11}^{(2)} = 6.252$, $a_{13}^{(2)} = 4.25$, $a_{33}^{(2)} = 5.25$, $a_{44}^{(2)} = 1.00$, $a_{66}^{(2)} = 2.25$.	Medium 1 : 0.28, ±0.31, ±0.45, ±0.54 Medium 2 : ±0.25, ±0.27, ±0.42 ±0.63

(a)
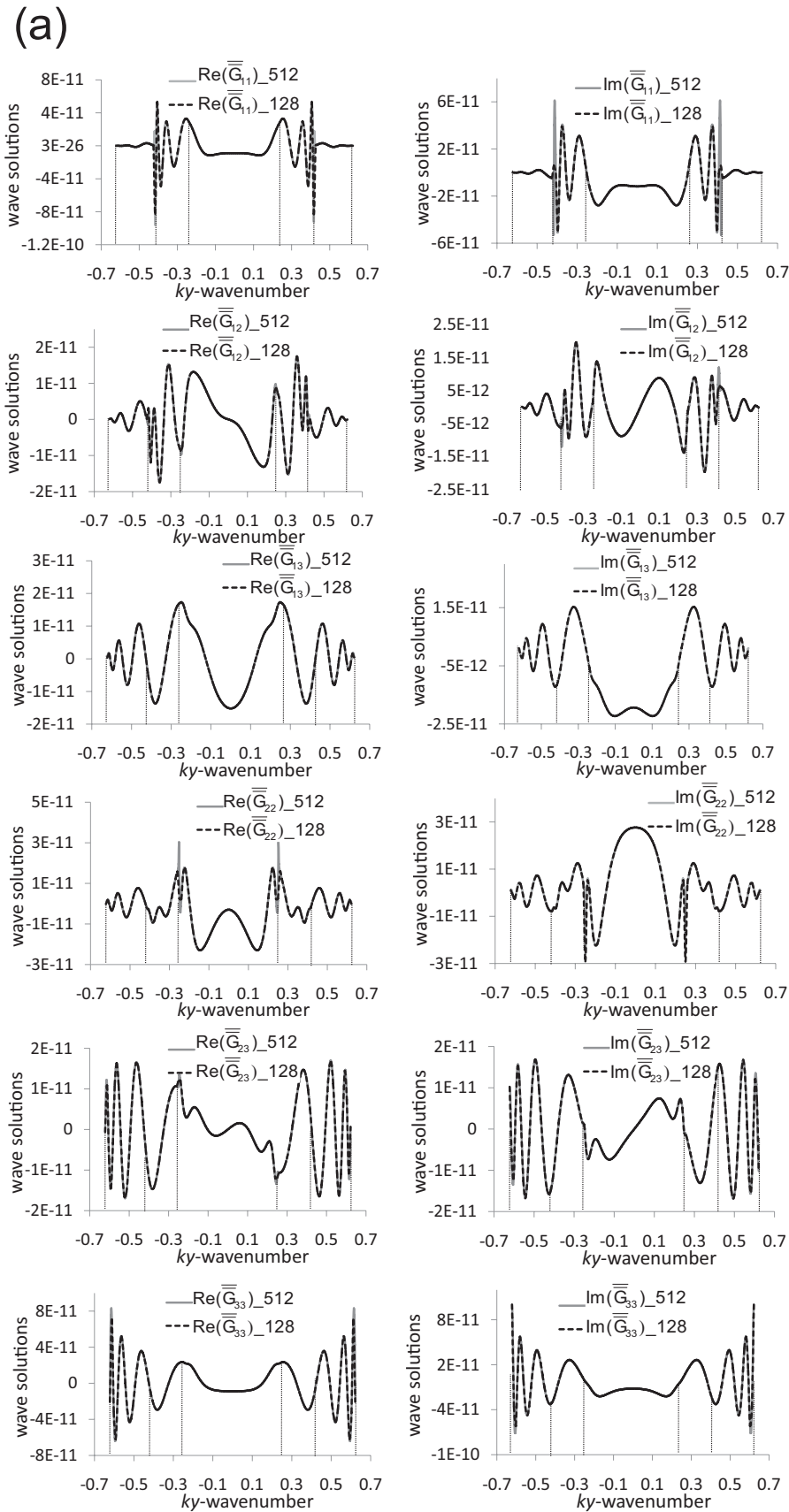
Figure 3. The real and imaginary parts of the wavenumber-domain solutions in a full-space homogeneous, anisotropic medium (see Table 1) at two offsets: (a) $r = 28.3$ m and (b) $r = 212$ m. The vertical lines at wavenumbers ±0.25, ±0.48 and ±0.63 denote the critical wavenumbers.
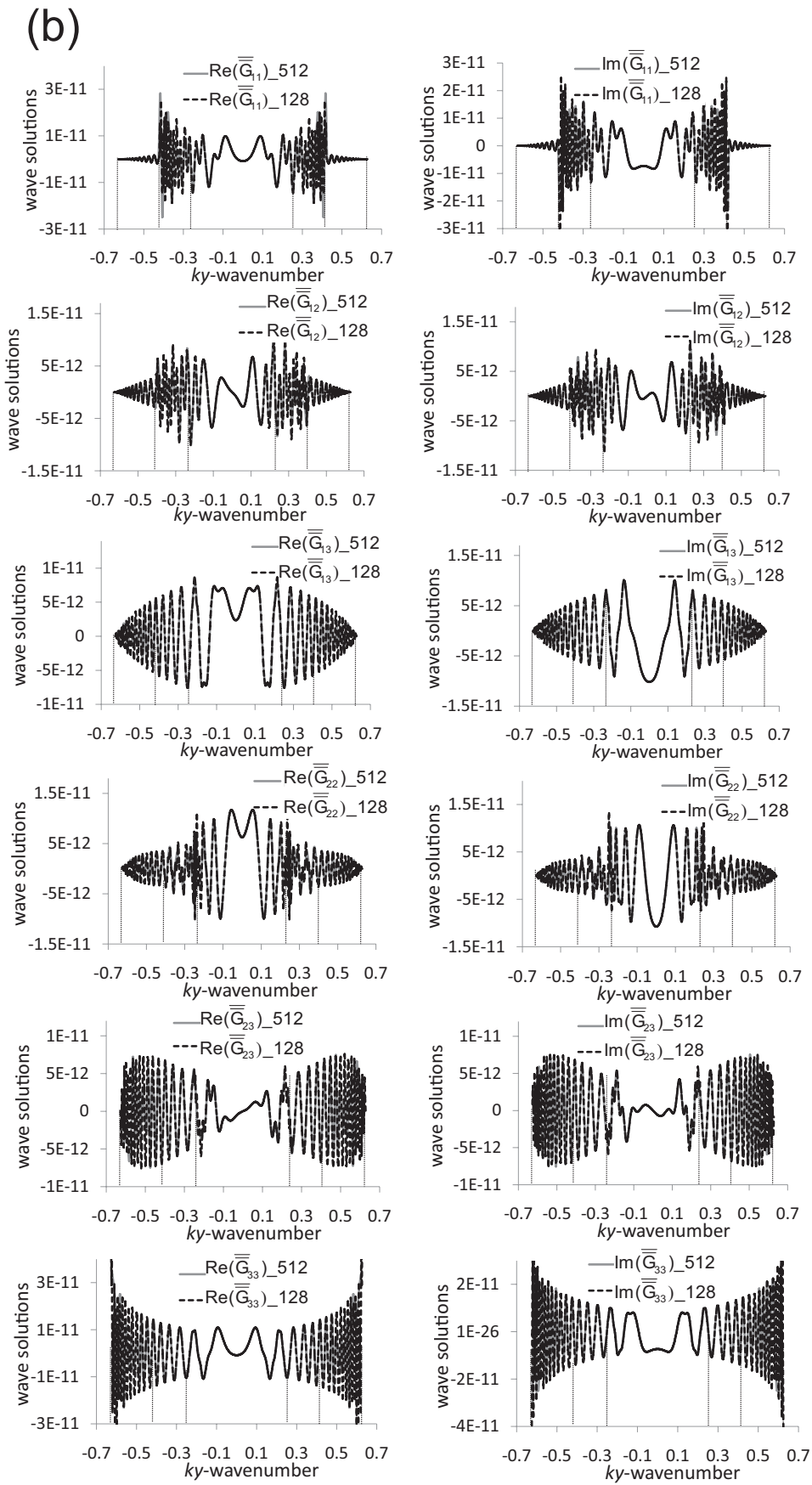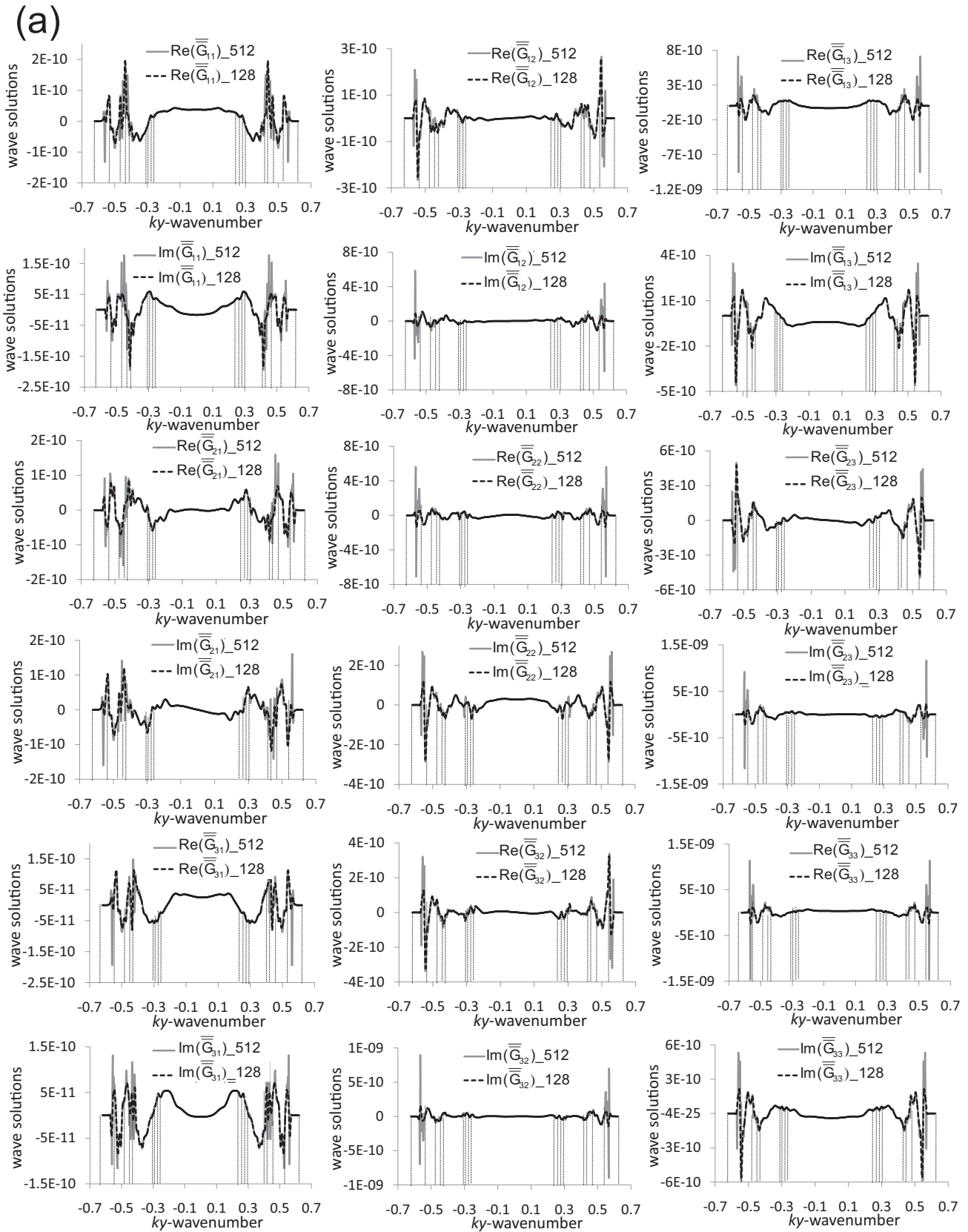
Figure 3. (*Continued.*)

(a)

Figure 4. The real and imaginary parts of the wavenumber-domain solutions for the two-layered anisotropic model (see Table 1 and Fig. 2) at two depths: (a) geophone 1 and (b) geophone 2, as shown in Fig.2. Note the eight critical wavenumbers in both the positive and negative k_y directions, indicated by the vertical lines.
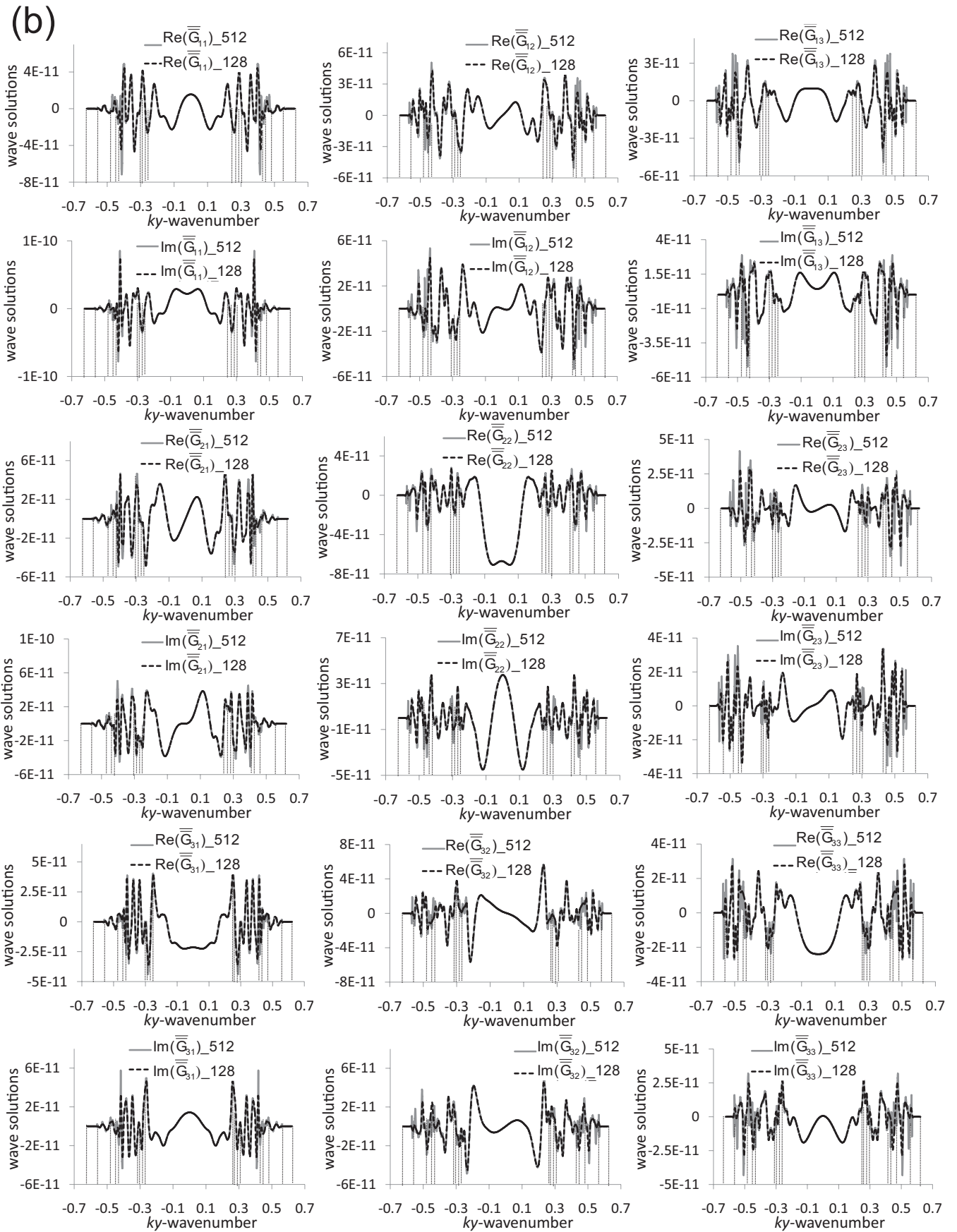
Figure 4. (*Continued.*)

antisymmetric properties of the components that have been given by eq. (14). (2) The 128- and 512-sampling schemes yield consistent results, but the former consumes one-third the computer time of the latter and it implies that choosing an appropriate number of the samples may significantly improve the efficiency of the 2.5-D modelling technique. (3) All the curves exhibit continuous behaviour at the singularity positions, particularly see Fig. 4 where there are 16 singularities over the wavenumber domain. This means that even slight attenuation ($\varepsilon = 10^{-12}$) removes the singularities. (4) The oscillations of the curves increase with increasing wavenumber and increasing offsets. See, for example Fig. 3(a), which is a simple case of an anisotropic medium and has six singularities at ± 0.25, ± 0.42 and ± 0.63. It can be observed that the oscillatory behaviour of the curves at the end-parts of each interval (± 0.42, ± 0.63) is of higher frequency than in the mid-part ($-0.25, 0.25$). Further, by comparing Fig. 3(a) (offset $r = 28.3$ m) and Fig. 3(b) (offset $r = 212$ m), one finds that as the offset increases, the oscillation frequency at the end-parts of the wavenumber interval increases as well. Such characteristics are also visible in Fig. 4, corresponding to the heterogeneous, anisotropic case.

According to these characteristics, we can construct the sampling strategies valid for these cases, that is, based on the singularity-skipping strategy (Zhou & Greenhalgh 2006), we replace eq. (16) with the following formula for the irregular sampling approach:

$$N_{ky} = \sum_{q=1}^{N_s^e} \max\left\{5, \text{int}\left[2c^{N_s-q} \cdot \left(\frac{2r_{\max}}{\lambda_{\max}}\right)\right]\right\}, \quad c < 1, \quad (19)$$

where we take the double integer $\text{int}[2r_{\max}/\lambda_{\max}]$ as the number of samples in the end-part of the intervals and decrease it by the factor c^{N_s-q} in the descent direction. It shows N_{ky} is proportional to k_y^c, frequency $f = \max(\sqrt{a_{pp}^{(m)}})/\lambda_{\max}$ and offset $r_{\max}$ so that the strategy basically satisfies the sampling requirements for different ranges of k_y, source–receiver offsets and frequencies. Apparently, this strategy is not unique, but one can experimentally determine the factor c to yield satisfactory results with N_{ky} as small as possible.

We set $c = 1/2$, used eq. (19) and obtained $N_{ky} = 38$ and $N_{ky} = 63$ for the two models. We recalculated the wavefields and showed that the solutions with the 38-wavenumber samples match very well with the analytic solutions in the homogenous anisotropic model (omitted here). As an example, we present Fig. 5 which shows the solutions for the two-layered anisotropic model given in Table 1. Because no analytic solution is available for comparison, we plotted the results obtained by the irregular sampling strategy ($N_{ky} = 63$) against the solutions obtained by the denser regular sampling strategy ($N_{ky} = 256$). It shows that the irregular sampling strategy produces consistent results with those obtained by the dense sampling, but the former takes only one-fourth as much computer time compared to the latter. These experiments confirm that employing an appropriate sampling strategy can significantly improve the computational efficiency of 2.5-D seismic wave modelling in the frequency domain.

To show the differences between the 2.5-D (point source) and 2-D (line source) frequency-domain wave modelling, we repeated the above experiments with a line source, whose solution is defined by eq. (1) with $k_y = 0$ and obtained by solving the linear system eq. (6) with such zero wavenumber. Fig. 6 gives five independent non-zero components of the Green's function tensors along the free surface of the two-layered anisotropic model, together with the previous 2.5-D modelling results shown in Fig. 5. For ease of comparison, we multiplied the 2-D results with the factor $1/\sqrt{r}$. These

diagrams show the differences in the amplitude and the phase of the wavefields at the specified frequency (100 Hz). The 2.5-D wavefield spreads roughly spherically (as $1/r$) but the 2-D wavefield does not (it spreads cylindrically, or roughly as $1/\sqrt{r}$) so multiplying the 2-D results with the factor $1/\sqrt{r}$ should approximately equalize the amplitudes (the correction is strictly valid only in the far-field for a homogenous acoustic full-space). But even after such correction, the components of the 2-D numerical results give a poor match with the amplitudes of the 2.5-D numerical modelling, particularly in the heterogeneous anisotropic medium (see Fig. 6). One also can see the phase delays in the 2.5-D numerical results compared with the 2-D modelling solutions. The phase difference between 2.5-D and 2-D frequency-domain wavefields has already been pointed out by Williamson & Pratt (1995), who showed a $\pi/4$ phase difference between the 2.5-D and 2-D solutions in the far-field situation for a uniform acoustic medium. These experiments clearly show that simple conversion from the 2-D to 2.5-D wavefields cannot guarantee the correct dynamic features in complex anisotropic media. To further verify the 2.5-D modelling schemes, we employed our 3-D frequency-domain modelling code (Zhou & Greenhalgh 2011) for the two-layered anisotropic model and obtained Fig. 7, which gives the 2.5-D and 3-D modelling results along the undulating surface topography and shows the consistent results for the 3-D wavefield over the 2-D geological model.

To demonstrate the capabilities of the 2.5-D modelling strategies for a practical geological model, we calculated five non-zero components $\{\overline{G}_{11}, \overline{G}_{13}, \overline{G}_{22}, \overline{G}_{31}, \overline{G}_{33}\}$ of the displacement vector at a frequency of 1 Hz (see Fig. 8) for a subduction-type model (shown by the black lines in the wavefield images in Fig. 8). The elastic moduli of the subduction zone are given in Table 2. The point source is located at the middle of the model 25 km below the free surface. From Table 2 and the specified frequency, one finds that the minimum wavelength is $\lambda_{\min} = 3.2$ km, the cut-off wavenumber is $k_y^c \approx 0.0196$ and the maximum source–receiver offset distance is $r_{\max} = 100$km. Accordingly, for these calculations we choose seven points over the minimum wavelength as the model-discretization density and the regular sampling strategy of $N_{ky} = 290$ wavenumbers. Due to the limitation of our computer memory, we could not implement full 3-D simulation of the subduction model for comparison (Table 3), but we repeated the computations with more dense wavenumbers ($N_{ky} = 512$) to check the stability of the solutions. In Fig. 8, we also give the profiling curves along the free surface of the wavefields as obtained by the two sampling strategies and once again show the consistent solutions. The computational efficiency of the 2.5-D scheme was achieved by appropriately choosing the wavenumber samples. From the five wavefield images given in Fig. 8, one can observe the characteristics of the wavefields, for example, different wave-propagating patterns in the layers due to different source directions and strong interferences of the reflections, refractions and guided waves in the layers. From the free-surface profiling curves, one also can see significant changes of the magnitudes of the displacement vectors over the two tectonic plates of the subduction model.

Table 3 lists the computer memory and CPU time costs (SGI Altix XE 1300) for the above three models. As mentioned above, due to the memory limitation of the computer, we could not perform full 3-D computations with the same matrix solver (LU-decomposition) as used in the 2.5-D schemes because of dramatic increase in the computer memory with the dimensions of the matrix. Therefore, we had to employ an iterative linear-system solver (Zhou & Greenhalgh 2010) that consumes far less computer memory than the matrix solver. From Table 3, one can see the computational benefits of the
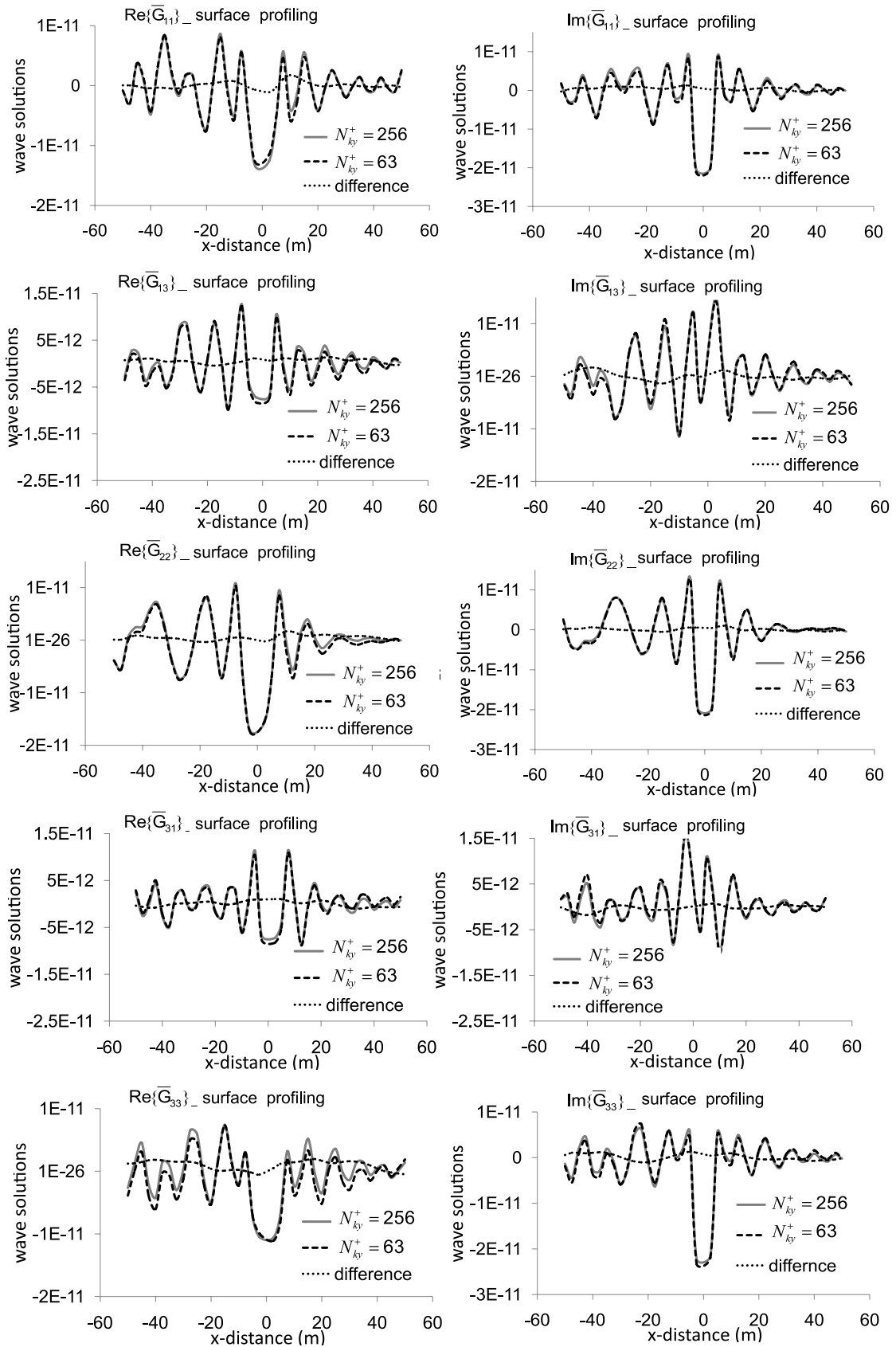
Figure 5. Five independent components of the numerical wave solutions yielded by the irregular sampling strategy ($N_{ky} = 63$) and the regular sampling strategy ($N_{ky} = 256$) at $f = 100$ Hz along the undulating free-surface topography of the two-layered anisotropic model given in Table 1.
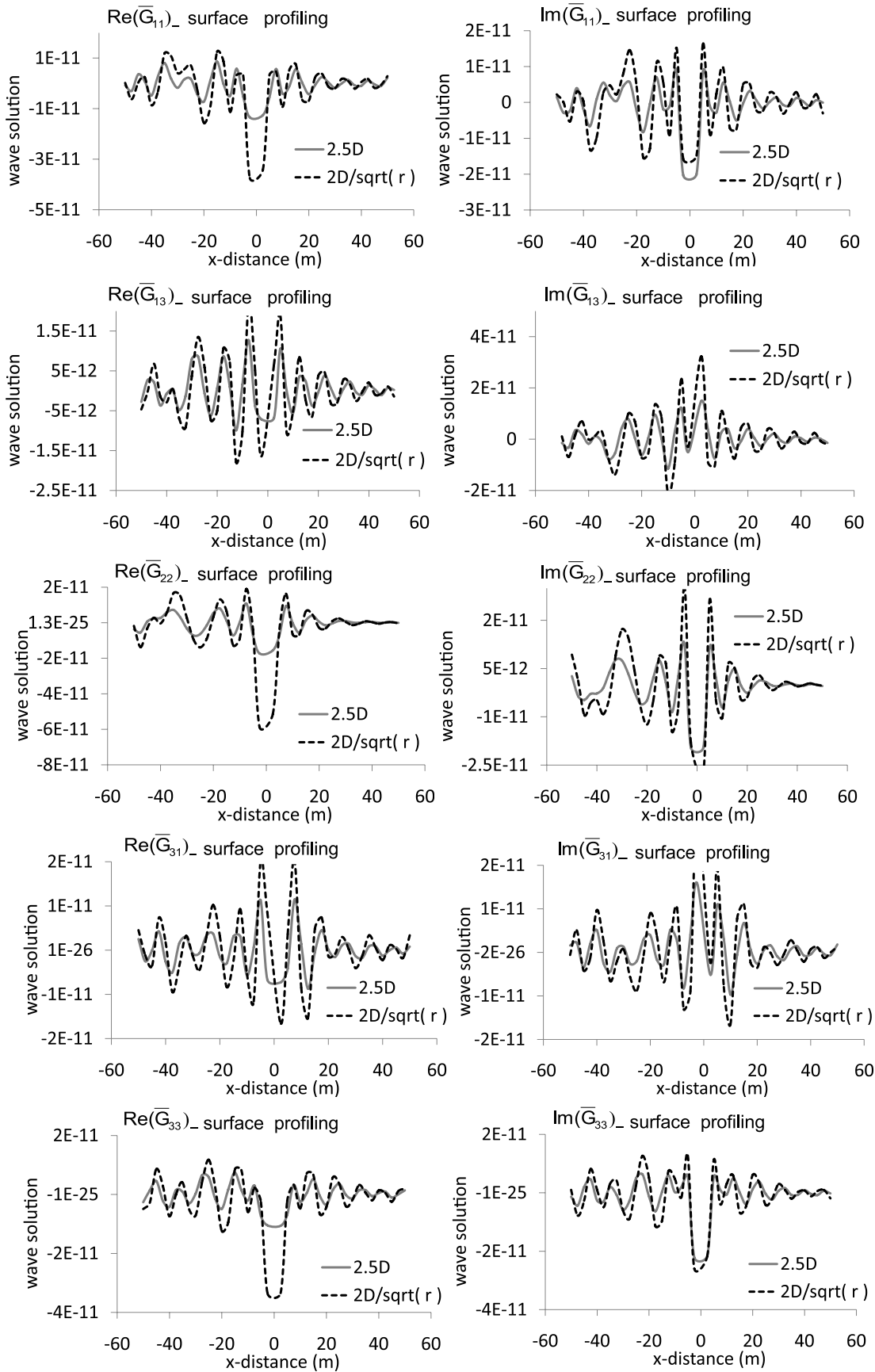
Figure 6. Comparisons of the 2.5-D and 2-D wave solutions at 100 Hz in the two-layered anisotropic model given in Table 1.
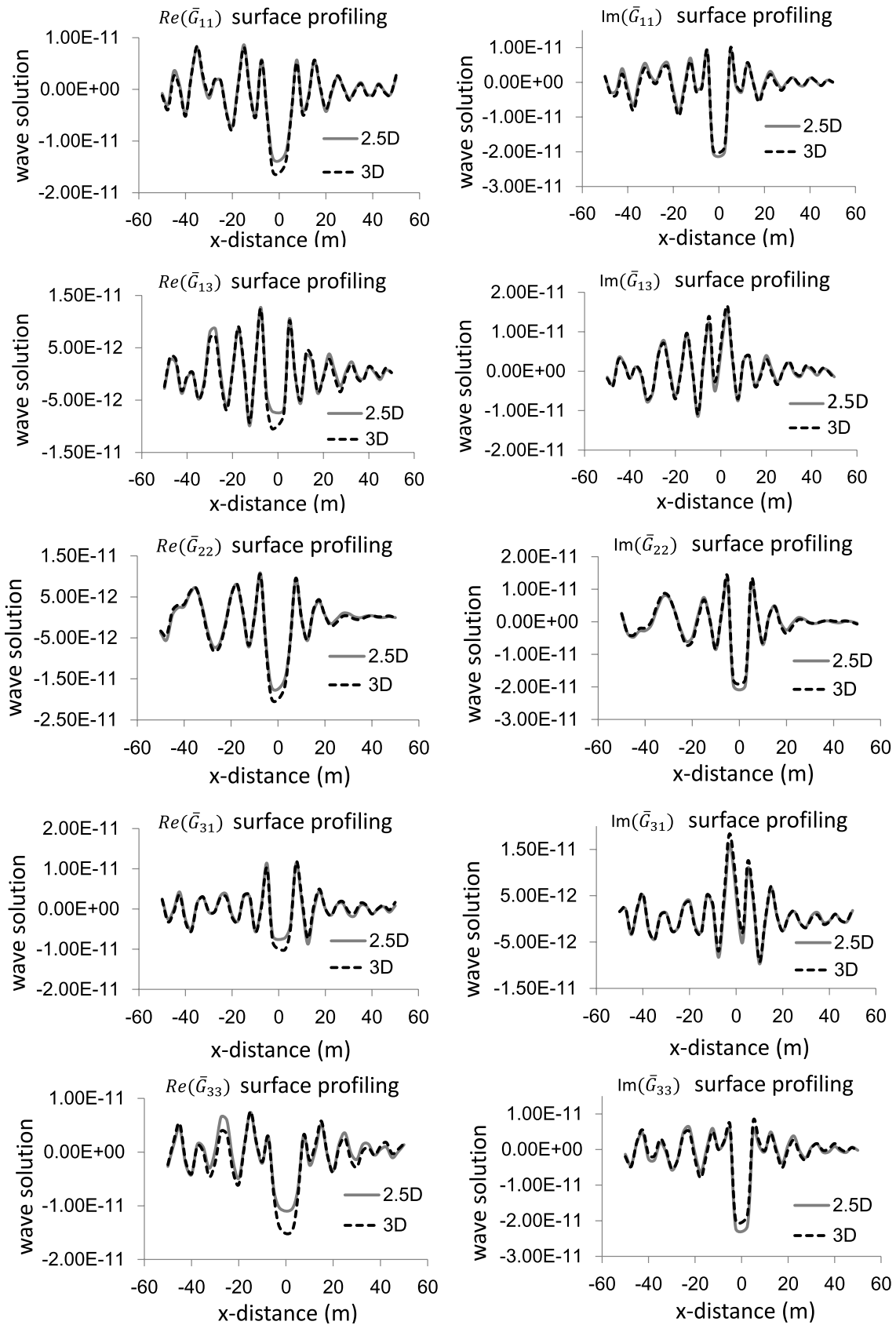
Figure 7. Numerical solutions of the 2.5-D (regular sampling scheme) and 3-D frequency-domain wave modelling at 100 Hz in the two-layered anisotropic model given in Table 1.
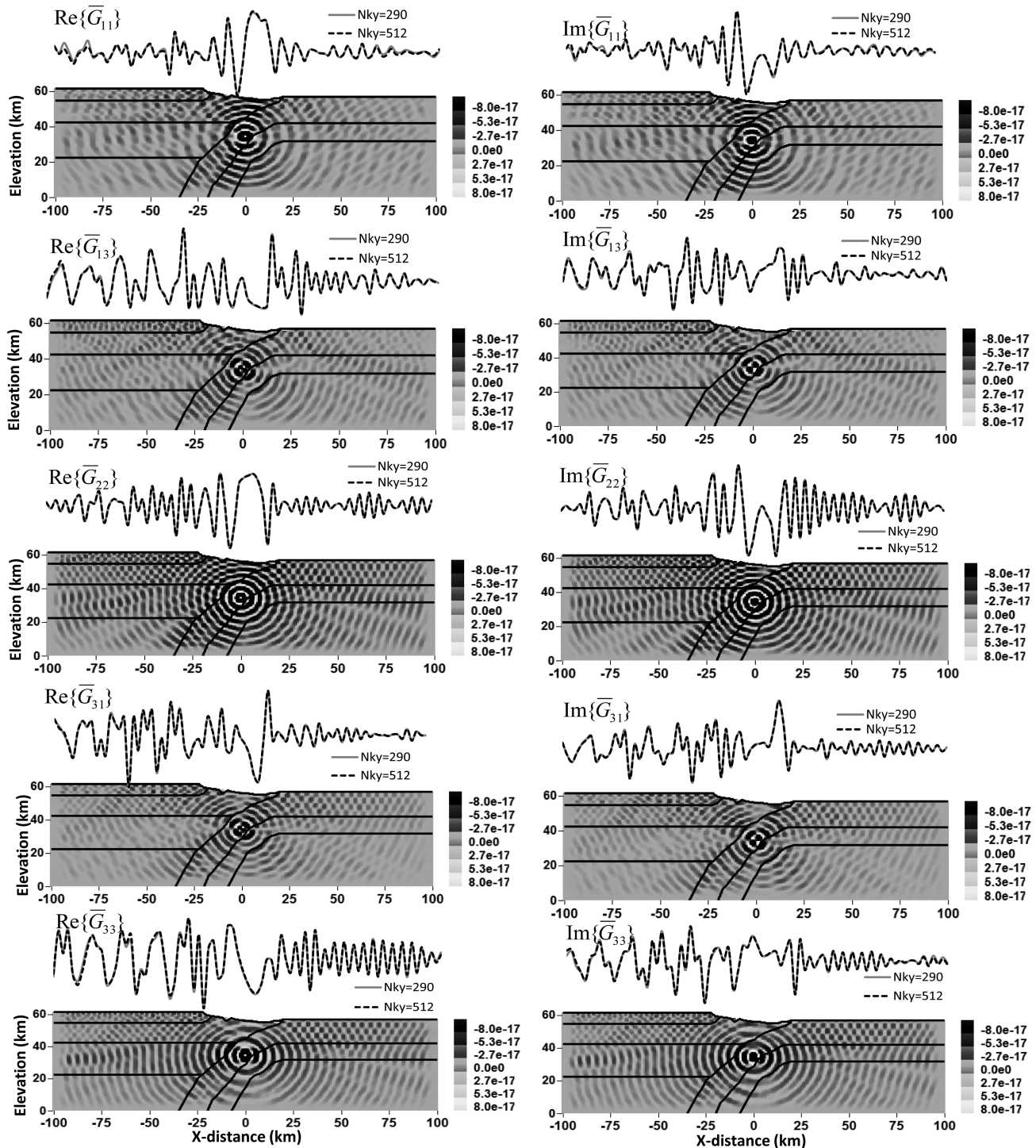
Figure 8. 2.5-D frequency-domain numerical solutions for a subduction zone model. The model parameters are given in Table 2. The frequency is 1 Hz and seven points over the minimum wavelength were employed in the computations.

2.5-D schemes for simulating the 3-D wavefields in a 2-D geological model.

CONCLUSIONS

We have demonstrated two effective wavenumber sampling schemes, called the irregular and regular sampling strategies, for 2.5-D frequncy-domain seismic wave modelling. The former is an

extension of our previous singularity-skipping strategy for acoustic media to general, anisotropic media, whereas the latter is achieved by the introduction of slight attenuation in the model to remove the singularities at the critical wavenumbers, to completely overcome the singularity problem.

We show both mathematically and numerically that the Green's function vector wavenumber-domain solutions in the 2.5-D general anisotropic case are symmetric or antisymmetric about the wavenumber axis, and that the oscillatory behaviour of the spectral

Table 2. Elastic moduli for the subduction model shown in Fig. 8.

Tectonic plate 1	Elastic moduli (ρ: kg m^{-3}; c_{ij}: 10^9m^2 s^{-2})	Tectonic plate 2	Elastic moduli (ρ: kg m^{-3}; c_{ij}: 10^9m^2 s^{-2})
Layer 1	$\rho = 2500$, $c_{11} = 75.625$ $c_{13} = 24.425$, $c_{33} = 75.625$ $c_{44} = 25.60$, $c_{66} = 25.60$	Layer 1	$\rho = 3300$, $c_{11} = 161.7$ $c_{13} = 50.754$, $c_{33} = 177.87$ $c_{44} = 61.025$, $c_{66} = 55.473$
Layer 2	$\rho = 2900$, $c_{11} = 122.525$ $c_{13} = 38.773$, $c_{33} = 122.525$ $c_{44} = 41.876$, $c_{66} = 41.876$	Layer 2	$\rho = 3500$, $c_{11} = 194.063$ $c_{13} = 60.479$, $c_{33} = 213.46$ $c_{44} = 73.471$, $c_{66} = 66.792$
Layer 3	$\rho = 3500$, $c_{11} = 194.06$ $c_{i3} = 60.479$, $c_{33} = 213.46$ $c_{44} = 73.471$, $c_{66} = 66.792$	Layer 3	$\rho = 3900$, $c_{11} = 249.6$ $c_{13} = 77.298$, $c_{33} = 274.5$ $c_{44} = 94.766$, $c_{66} = 86.151$
Layer 4	$\rho = 3900$, $c_{11} = 249.6$ $c_{13} = 77.298$, $c_{33} = 274.5$ $c_{44} = 94.766$, $c_{66} = 86.151$		

Table 3. Computer memory and CPU-time costs of 2.5-D and 3-D frequency-domain seismic wave modelling. The matrices for the 2.5-D cases are stored in banded form and the system solved by the LU decomposition approach. The matrices in the 3-D cases are stored only as non-zero elements and solved by the BiCG-solver.

Model	2.5-D			3-D		
	Grid	Memory (GB)	CPU-time (hr)	Grid	Memory (GB)	CPU-time (hr)
Homogenous	161×161	3.7	3	$161 \times 161 \times 161$	24	113
Two-layered	145×177	3.9	5.1	$145 \times 177 \times 177$	26	126
Subduction	137×433	6.7	47	$137 \times 433 \times 433$	36	Not applicable

amplitudes increases with increasing wavenumber and increasing source–receiver offset. The two presented strategies fully take into account such properties and characteristics of the wavenumber-domain solutions, so that they significantly reduce the cost of computer memory and run time, thus enhancing the computational efficiency of 2.5-D frequency-domain seismic wave modellingwhile retaining satisfactory accuracy.

The irregular sampling strategy uses Gauss–Legendre abscissa sampling in the wavenumber domain so as to avoid the singular wavenumber points. It requires that the singular wavenumber positions be known in advance from the given frequency and the diagonal elements of the Voigt recipe for the density-normalized elastic modulus tensor. It is particularly suitable for cases where the number of singularities may be controlled in the computation. The regular sampling strategy distributes the wavenumber samples uniformly over the wavenumber domain and may be applied to non-linear diffraction tomography and frequency-domain full-waveform inversion where the number and positions of the singularities are not known in advance and can hardly be controlled in the iterative model up-grading.

From these numerical experiments, it is apparent that the 2.5-D frequency-domain modelling scheme is applicable for computing the frequency-domain wavefield solutions and the sensitivity kernels (see examples, Zhou & Greenhalgh 2011) at the dominant frequencies employed in non-linear seismic diffraction tomography or frequency-domain full-waveform inversion in anisotropic media.

ACKNOWLEDGMENTS

REFERENCES

Aki, K. & Richards, P., 2002. *Quantitative Seismology: Theory and Methods,* Vols I & II, W.H. Freeman & Co, San Francisco, CA

Becker, E.B., Carey, G.F. & Oden, J.T., 1983. *Finite elements: A Second Course,* Vol. **II**, Prentice-Hall, Inc, Englewood Cliffs.

Furumura, T. & Takenaka, H., 1996. 2.5-D modelling of elastic waves using the pseudo-spectral method, *Geophys. J. Int.,* **124,** 820–832.

Gelius, L.J., 1995. Generalized acoustic diffraction tomography, *Geophys. Prospect.,* **43,** 3–29.

Kelley, K.R. & Marfurt, K.J., 1990. *Numerical Modeling of Seismic Wave Propagation,* Geophysics Reprints Series No. 13, Soc. Exploration Geophysicists, Tulsa, OK.

Mallick, S. & Frazer, L.N., 1987. Practical aspects of reflectivity modelling, *Geophysics,* **52,** 1355–1364.

Novais, A. and Santos, I.T., 2005. 2.5D finite difference solution of the acoustic wave equation, *Geophys. Prospect.,* **53,** 523–531.

Pedersen, H.A., Sànchez-Sesma, F. J. & Campillo, M., 1994, Three-dimensional scattering by two-dimensional topographies, *Bull. seism. Soc. Am.,* **94,** 1169–1183.

Pedersen, H.A., Maupin, V. & Campillo, M. 1996, Wave diffraction in multi-layered media with the indirect boundary element method. Application to 3D diffraction of long period surface waves by 2D lithospheric structures, *Geophys. J. Int.,* **125,** 545–558.

Pratt, R.G., 1999. Seismic waveform inversion in the frequency-domain. Part 1: theory and verification in a physical scale model, *Geophysics,* **64,** 902–914.

Press, W.H., Tenkolsky, S.A., Vetterling, W.T. & Flannery, B.P., 1986. *Numerical Recipes in Fortran, the Art of Scientific Computation,* Cambridge University Press, Cambridge.

Rocker, S., Baker, B. & McLaughlin, J., 2010. A finite-difference algorithm for full waveform teleseismic tomography, *Geophys. J. Int.,* **181,** 1017–1040.

Sinclair, C., Greenhalgh, S. & Zhou, B., 2007. 2.5D modelling of elastic waves in transversely isotropic media using the spectral element method, *Explor. Geophys.,* **38,** 225–234.

Sinclair, C., Greenhalgh, S. & Zhou, B., 2011. Wavenumber sampling issues in 2.5-D frequency domain seismic modelling, *Pure appl. Geophys.,* in press, doi:10.1007/s00024-011-0277-3.

Song, Z.M. & Williamson, P.R., 1995. Frequency-domain acoustic wave modelling and inversion of cross-hole data. Part I—2.5D modelling method, *Geophysics,* **60,** 784–795.

Thomsen, L., 1986. Weak elastic anisotropy, *Geophysics,* **51,** 1954–1966.

Vavrycuk, V., 2007. Asymptotic Green's function in homogeneous anisotropic viscoelastic media, *Proc. R. Soc. A,* **463,** 2689–2707

Williamson, P. R. & Pratt, R. G., 1995. A critical review of the acoustic wave modelling procedure in 2.5 dimensions, *Geophysics,* **60,** 591–595.

Xu, K., Zhou, B. & McMechan, G.A., 2010. Implementation of pre-stack reverse-time migration using frequency-domain extrapolation, *Geophysics,* **75,** S61–S72.

Zhou, B. & Greenhalgh, S.A., 1998a. A damping method for the computation of the 2.5-D Green's function for arbitrary acoustic media, *Geophys. J. Int.,* **133,** 111–120.

Zhou, B. & Greenhalgh, S.A., 1998b. Composite boundary-valued solution of the 2.5D Green's function for arbitrary acoustic media, *Geophysics,* **63,** 1813–1823.

Zhou, B. & Greenhalgh, S.A., 1999. Explicit expressions and numerical calculations for the Fréchet and second derivatives in 2.5D Helmholtz equation inversion, *Geophys. Prospect.,* **47,** 443–468.

Zhou, B. & Greenhalgh, S.A., 2006. An adaptive wavenumber sampling strategy for 2.5D seismic-wave modelling in the frequency-domain, *Pure appl. Geophys.,* **163,** 1399–1416.

Zhou, B. & Greenhalgh, S.A., 2011, Computing the sensitivity kernels for 2.5-D seismic waveform inversion in heterogeneous, anisotropic media, *Pure appl. Geophys.,* **168,** 1729–1748, doi:10.1007/s00024-010-0191-0.

Zhou, B. & Greenhalgh, S.A., 2011. 3-D frequency-domain seismic wave modelling in heterogeneous, anisotropic media using a Gaussian quadrature grid approach, *Geophys. J. Int.,* **184,** 507–526.